Journal of Materials Chemistry C

ROYAL SOCIETY OF CHEMISTRY

PAPER

View Article Online
View Journal | View Issue

Cite this: J. Mater. Chem. C, 2020, 8, 3773

Exciton efficiency beyond the spin statistical limit in organic light emitting diodes based on anthracene derivatives†‡

Nidhi Sharma,§[ab] Michael Yin Wong,§[a] David Hall,[ac] Eduard Spuling,[a] Francisco Tenopala-Carmona,[b] Alberto Privitera,[d] Graeme Copley,[a] David B. Cordes,[a] Alexandra M. Z. Slawin,[a] Caroline Murawski,¶[b] Malte C. Gather,[b] David Beljonne,[c] Yoann Olivier,*[ce] Ifor D. W. Samuel*[b] and Eli Zysman-Colman*[a]

Received 19th November 2019,
Accepted 27th January 2020

DOI: 10.1039/c9tc06356k

rsc.li/materials-c

We report two donor–acceptor (D–A) materials based on a cyanoanthracene acceptor paired with diphenylamine (**DPAAnCN**) and carbazole (**CzAnCN**) donor moieties. These compounds show hybrid locally excited (LE) charge-transfer (CT) excited states (HLCT), which we demonstrated through a combined photophysical and computational study. Vacuum-deposited organic light emitting diodes (OLEDs) using these HLCT emitters exhibit maximum external quantum efficiencies (EQE_{max}) close to 6%, with impressive exciton utilization efficiency (Φ_s) of >50%, far exceeding the spin statistic limit of 25%. We rule out triplet–triplet annihilation and thermally activated delayed fluorescence as triplet harvesting mechanisms along with horizontal orientation of emitters to enhance light outcoupling and, instead, propose a "hot exciton" channel involving the nearly isoenergetic T_2 and S_1 states.

Introduction

Since the first discovery of electroluminescence (EL) in anthracene crystals by Kallmann and Pope,[1] and bilayer Organic Light Emitting Diodes (OLEDs) by Tang and VanSlyke,[2] OLEDs have vastly improved in performance to the point where they are on the brink of becoming the dominant technology for displays, and show enticing advantages as solid-state lighting devices. In EL devices, according to spin statistics, hole and electron recombination typically generates both singlet and triplet excitons in a 1 : 3 ratio.[3] For high efficiency devices, a key feature is to have materials capable of recruiting 100% of these excitons. When small molecule fluorescent emitters are used in OLEDs, the triplet excitons are lost as heat due to their excessively long excited-state lifetimes, which limits the internal quantum efficiency (IQE) of the device to 25%. Devices with organometallic phosphorescent emitters can achieve an IQE of 100% thanks to favourable intersystem crossing rates, k_{ISC}, mediated by the strong spin–orbit coupling of the heavy metal centre.[4] A major drawback to their use is the scarcity of the noble metals that underpin this class of emissive materials. Presently, there are two alternative exciton-harvesting mechanisms for organic compounds that offer the potential to expand beyond the 25% IQE offered by fluorophores: (1) triplet–triplet annihilation (TTA)[5] and (2) thermally activated delayed fluorescence (TADF).[6] The maximum IQE for TTA is 62.5% whereas for TADF it is as high as 100%. TADF emitter development has thus emerged as an effective avenue to achieve high performance in OLEDs. However, a drawback of devices employing these emitters is that they frequently suffer from large efficiency roll-offs at high current densities arising from the existence of long-lived excited state lifetimes in the microsecond or sometimes even in the millisecond regime.[7]

[a] Organic Semiconductor Centre, EaStCHEM School of Chemistry, University of St Andrews, St Andrews, KY16 9ST, UK. E-mail: eli.zysman-colman@st-andrews.ac.uk; Web: http://www.zysman-colman.com
[b] Organic Semiconductor Centre, SUPA School of Physics and Astronomy, University of St Andrews, St Andrews, KY16 9SS, UK
[c] Laboratory for Chemistry of novel materials, University of Mons, Place du Parc 20, B-7000 Mons, Belgium
[d] Clarendon Laboratory, Department of Physics, University of Oxford, Parks Road, Oxford OX1 3PU, UK
[e] Unité de Chimie Physique Théorique et Structurale & Laboratoire de Physique du Solide, Namur Institute of Structured Matter, Université de Namur, Rue de Bruxelles, 61, 5000 Namur, Belgium

† The research data underpinning this publication can be accessed at https://doi.org/10.17630/60521616-d3b5-4708-bb16-3fcbb33dbeee

‡ Electronic supplementary information (ESI) available: Synthesis, X-ray crystallography, Lippert–Mataga model, supplementary optoelectronic measurements, computational data, NMR spectra, HRMS, HPLC and EA reports. CCDC 1960941 and 1960942. For ESI and crystallographic data in CIF or other electronic format see DOI: 10.1039/c9tc06356k

§ These authors contributed equally.

¶ Present address: Kurt-Schwabe-Institut für Mess- und Sensortechnik e.V. Meinsberg, Kurt-Schwabe-Str. 4, 04736 Waldheim, Germany.

A third alternative approach has recently been explored where light emission occurs *via* a hot exciton mechanism.[8] Such a mechanism usually involves the lowest singlet excited state S_1 and a close-to-resonant triplet excited state T_n, with $n > 1$, both of which displaying hybrid charge transfer-locally excited (HLCT) character to ensure the best compromise between high singlet radiative decay rates, small energy separation and fast triplet-to-singlet conversion.[9] T_1, instead, has a localized (LE) character. Molecules emitting from the hot exciton channel usually possess a large energy gap between the HLCT-like T_n and LE-like T_1 states (0.5–1.0 eV), so that the conversion from T_n to S_1 competes favourably with internal conversion (IC) between T_n and T_1 thus providing an avenue for exciton utilization going beyond the spin statistical limit. Note that triplet upconversion from T_1 to S_1 is inactive in these systems, owing to the large energy gap between the lowest singlet and triplet excited states.

An HLCT-active molecular system is usually verified by measuring the molecular dipole moment in different polarity solvents, where the dipole moment of an HLCT-active molecule decreases modestly in low polarity solvents and increases measurably in high polarity solvents. This change in behavior is attributed to an increasing CT character of the emission in high polarity solvents, while in low polarity solvents the S_1 state possesses much more significant LE character. Thus, in solvents of moderate polarity a "hybrid state" possessing significant mixed LE and CT (HLCT) character exists, which seems to be a necessary condition for efficient hot triplet-to-singlet conversion.[10] Only a small number of materials showing such a hot exciton mechanism have been reported to date (see Fig. 1 for the chemical structures of the emitters reported in the literature). The first material identified as an emitter taking advantage of the hot exciton mechanism, **TPA-PPI**,[8a] consisted of a triphenylamine and an annelated benzimidazole as the donor and acceptor moieties, respectively. This compound exhibited a blue emission with λ_{PL} of 440 nm. Solvatochromic experiments confirmed the presence of the HLCT character of the S_1 excited state, and non-doped OLED devices with **TPA-PPI** exhibited an EQE_{max} of 5.0% with a modest Φ_s of 27% and CIE coordinates of (0.15, 0.11). A similar mechanism is invoked for an analogous emitter with a slight modification to the acceptor group, **TBPMCN** (λ_{PL} 460 nm).[9b] Non-doped OLEDs showed EQE_{max} of 7.8% with CIE coordinates of (0.16, 0.16) and exhibited an impressive Φ_s of 97%. To the best of our knowledge, the **TBPMCN** OLEDs remain the most efficient of those when referring to the hot exciton mechanism. Recently, another blue emitter with λ_{PL} of 432 nm (CIE: 0.15, 0.06) comprised of an unusual dicyanocarbazole acceptor and triphenylamine donors (emitter **4**) showed an EQE_{max} of 6.5%.[11] Very few reports have been published on green and red emitters. The most efficient of these was based on a benzothiadiazole acceptor and a carbazole donor (**CzP-BZP**, λ_{PL} 520 nm)[12] with an EQE_{max} of 6.95%, Φ_s of 48% and CIE coordinates of (0.34, 0.60). Upon changing the acceptor to naphthothiadiazole (**TPA-NZP**), the emission was shifted to the deep red with λ_{PL} of 634 nm and the corresponding OLEDs exhibited a low EQE_{max} of 2.8% albeit an impressive Φ_s of 90%.[9a] Furthermore, upon changing the donor to dimethylacridan (**NZ2Ac**), Φ_s increased to 93% and the OLEDs showed an EQE_{max} of 6.2% while maintaining the deep red emission with λ_{EL} of 612 nm.[13]

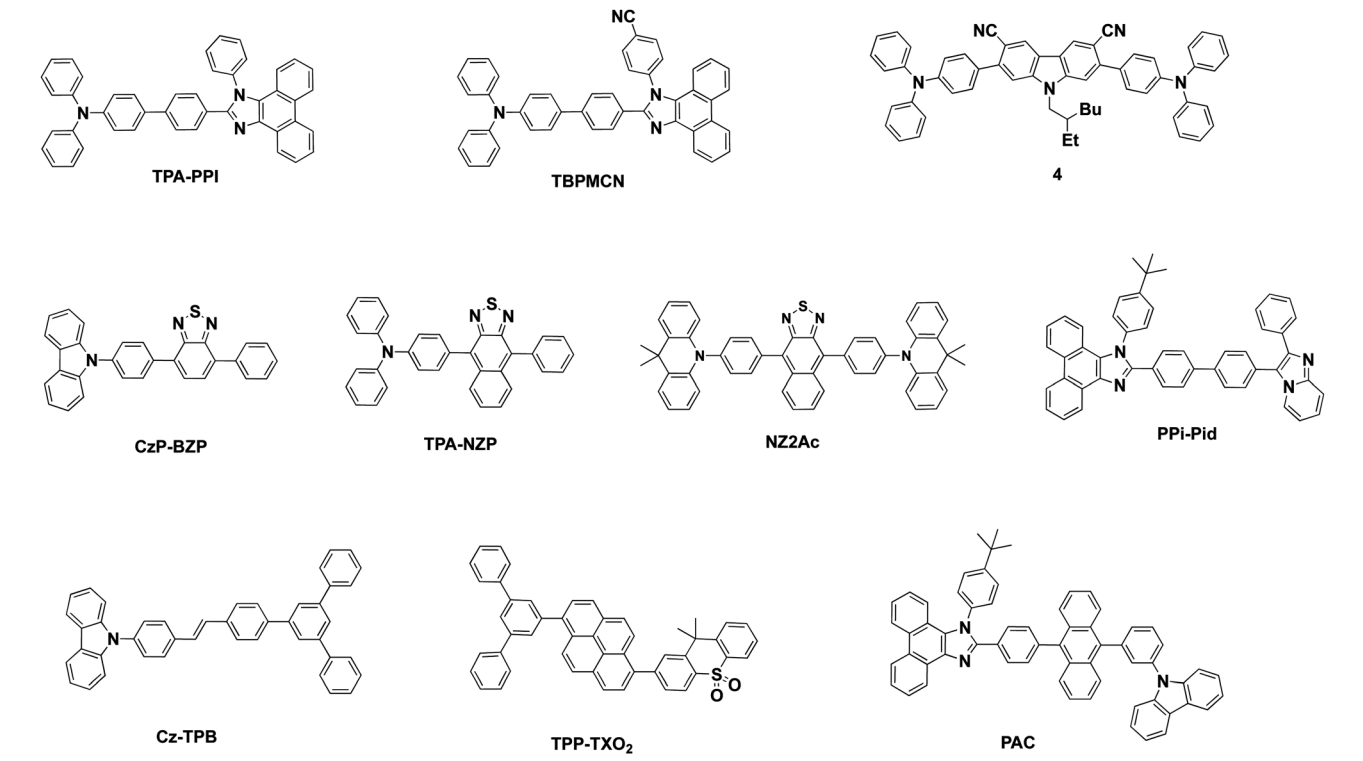

Fig. 1 Prior examples of emitters reported in the literature relying on the hot exciton mechanism.

Recently, the hot exciton mechanism approach has been explored to achieve deep blue emission in OLEDs. For example, emitter **PPi-Pid** exhibited blue emission with λ_{PL} = 473 nm and Φ_{PL} = 50% in the neat film.[14] The non-doped OLED showed deep-blue CIE coordinates of (0.15, 0.092) and Φ_s = 50%. The EQE_{max} was, however, low at 4.95%. Another deep-blue emitter **Cz-TPB** showed λ_{PL} = 435 nm and Φ_{PL} = 32% in the neat film.[15] The non-doped OLEDs maintained the deep blue emission with CIE coordinates of (0.15, 0.09) along with EQE_{max} and Φ_s of 4.32% and 87%, respectively. Both EQE_{max} and Φ_s were significantly improved when using emitter **TPP-TXO$_2$**, bearing pyrene as the bridging unit.[16] OLEDs with 12 wt% emitter doped in a double layer of TCTA and 26DCzPPy host matrices showed EQE_{max} of 10.5% and exhibited deep-blue emission with CIE coordinates of (0.15, 0.06) along with a tantalizing Φ_s of 100%. The deep-blue emitter **PAC** was recently reported.[17] The OLED using **PAC** displayed an EQE_{max} of 10.5%, CIE coordinates of (0.15, 0.06) and Φ_s of 100% in non-doped devices. The hot exciton channel was verified by transient absorption (TA) measurements, which revealed $\Delta E_{S_1-T_2}$ of 0.33 eV, high $\Delta E_{T_2-T_1}$ of 1.45 eV and high $\Delta E_{S_1-T_1}$ of 1.12 eV. This energy landscape facilitated a RISC channel from T_2 to S_1 over IC from T_2 to T_1. To date, **PAC** remains the only emitter where there is experimental evidence to support the hot exciton channel mechanism.

In this study, we have designed two novel cyanoanthracene emitters, **DPAAnCN** and **CzAnCN**, containing diphenylamino (DPA) and carbazole (Cz) donor groups, respectively (Fig. 2). The presence of the anthracene forces an increased torsion between groups substituted at the 9 and 10 positions compared to a *para*-disubstituted benzene. Secondly, the anthracene unit itself possesses excellent thermal stability and, unlike benzene bridges in TADF D–A emitters, it is photophysically non-innocent and thus can potentially enrich the optoelectronic properties of the emitter. Sufficiently large dihedral angles between the nitrogen-containing donors and the anthracene mediates mixing of LE and CT excited states while the presence of the anthracene group promotes a sufficiently large T_1–T_2 energy gap with T_1 being localized on the anthracene core. Through combined experimental and theoretical studies, we show that both compounds display exciton utilization largely surpassing the spin statistical limit, which we associate to a hot exciton channel after ruling out all other possible options. The use of anthracene within the emitter design has already been shown to be compatible with an HLCT material.[8b,18] For example, the compound **TPA-An** (Fig. 2), comprising an anthracene acceptor paired with a triphenylamine as the donor, has been shown through a combination of theoretical and solvatochromic experiments[8b] to be an emitter exploiting the hot exciton channel; however, both EQE_{max} and Φ_s remain low at 3% and 30%, respectively. Here we demonstrate that the substitution of the anthracene chromophore with a cyano group significantly affects the nature of the relevant excited states, leading to an optimised mixing of LE and CT character. As a result, both EQE_{max} and Φ_s exhibited a two-fold enhancement in **DPAAnCN** compared to **TPA-An**.

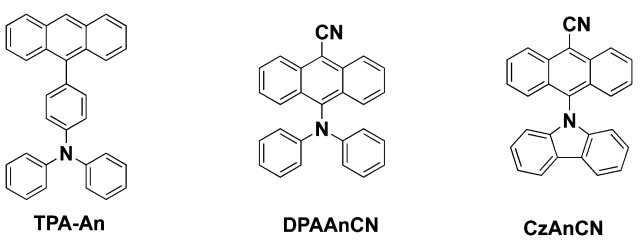

Fig. 2 Anthracene based D–A derivatives.

Results and discussion

Synthesis

Both **DPAAnCN** and **CzAnCN** were obtained *via* nucleophilic aromatic substitution of the corresponding amine donors, **D1–D2**, with the common intermediate 10-bromoanthracene-9-carbonitrile, **5** (Scheme S1, ESI‡). Both anthracene-based emitters were isolated and purified by a combination of column chromatography and recrystallization. Their structure and purity were confirmed by NMR, HPLC, HRMS, EA and single crystal structure analyses. X-ray quality crystals of these derivatives were grown by slow vapour diffusion, using either DCM and ether (**DPAAnCN**) or toluene and hexane (**CzAnCN**) as solvents and antisolvents. Their crystal structures are shown in Fig. 3. There is a large torsion between the donor groups and the cyanoanthracene acceptor moiety, which is caused by the increased steric hindrance conferred by the anthracene moiety. The dihedral angle between the donor and cyanoanthracene for **DPAAnCN** and **CzAnCN** are 81.10(16)° (for torsion angle C15–N1–C1–C2) and 64.0(2)° (for torsion angle C27–N15–C1–C2), respectively.

Molecular design

We have characterized the excited state properties of both compounds using density functional theory (DFT) calculations considering the PBE0 functional[19] with the 6-31G(d,p) basis set. We have first optimized the ground state of both derivatives. Then, based on these geometries, we have carried out linear-response time-dependent (TD-)DFT calculations within the Tamm–Dancoff approximation (TDA),[20] which significantly and systematically improves the accuracy of triplet energies and thus ΔE_{ST}.[21] In the ground state, **CzAnCN** showed a twist angle of 72°, which is in rather good agreement with the obtained crystal structure [64.0(2)°] (Fig. 3a). On the other hand, the twist angle for the **DPAAnCN** was 66° as predicted by DFT and 81.10(16)° according to the crystal structure analysis (Fig. 3b). Compared with **CzAnCN**, the large twist angle in the crystal structure of **DPAAnCN** can be attributed to the repulsion between the two phenyl rings in the diphenylamine moiety. Due to the strong electron-withdrawing ability of the anthracene-9-carbonitrile group, the lowest unoccupied molecular orbital (LUMO) is mainly localised on the acceptor moiety in both derivatives. The highest occupied molecular orbital (HOMO) of the two derivatives is delocalized over both the donor and acceptor moieties.

An attachment/detachment formalism was used to obtain the hole and electron densities associated with each singlet and

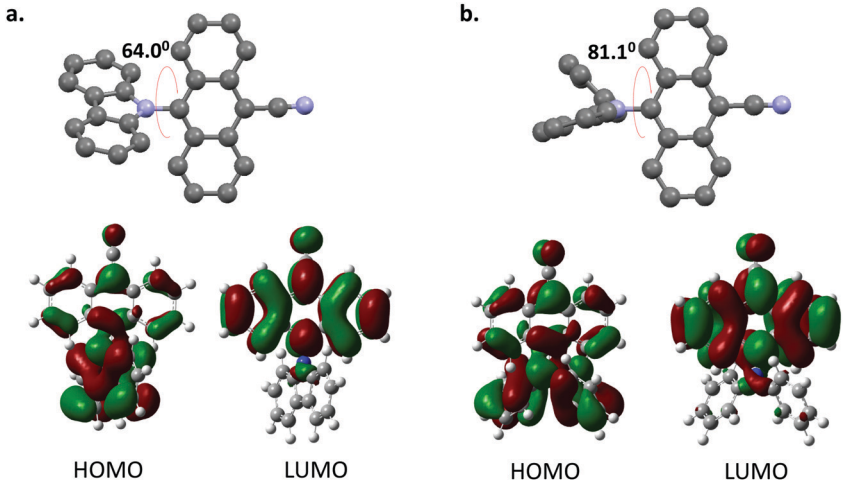

Fig. 3 Crystal structures (thermal ellipsoids at the 50% probability level) and HOMO–LUMO diagram of (a) **CzAnCN** and (b) **DPAAnCN**.

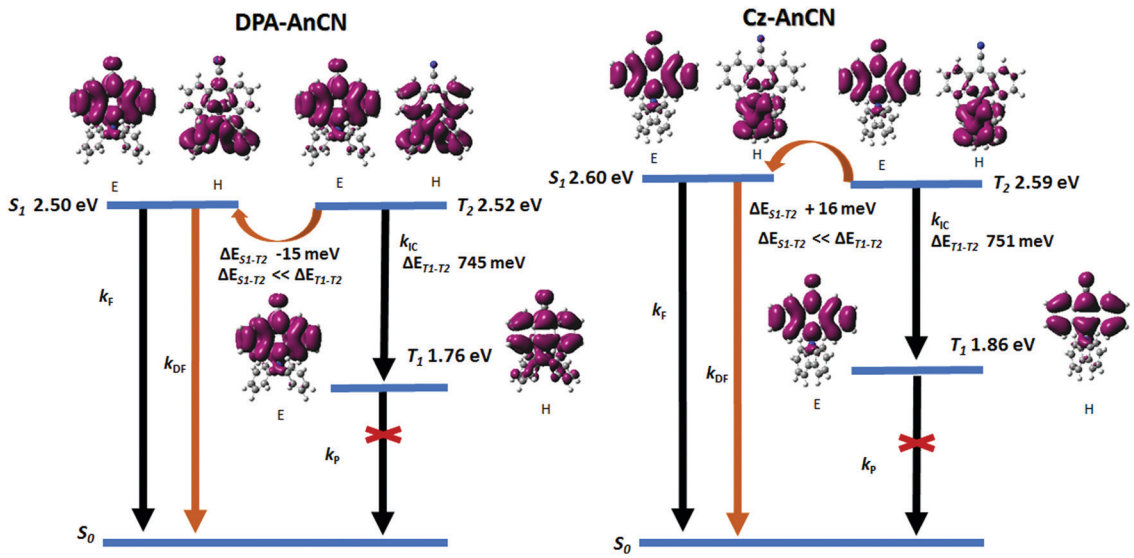

Fig. 4 Excited state energy diagram of **DPAAnCN** and **CzAnCN**. E and H correspond to the electron and hole densities computed in the attachment/detachment formalism. k_F, k_{DF}, k_P, k_{IC} correspond to the fluorescence, delayed fluorescence, phosphorescence and internal conversion rates, respectively. $\Delta E_{S_1-T_2}$ ($\Delta E_{T_1-T_2}$) are the energy differences between S_1 (T_1) and T_2.

triplet excited states and η_S, the overlap between the hole and electron densities. This formalism offers a clear picture of the nature of the excited states. Fig. 4 gives a pictorial description of the "hole" and "electron" in **DPAAnCN** and **CzAnCN**, respectively. For the $S_0 \rightarrow S_1$ transition in **DPAAnCN**, the hole is mainly localized on the donor moiety whereas the electron is mainly located on the AnCN acceptor. CT excitation from DPA to AnCN provides a dominant contribution to the S_1 and T_2 excited-state wavefunctions, yet these should be viewed as HLCT states as testified by the calculated η_S values. In contrast, T_1 with η_S values larger than 0.8 is of clear LE character (see Table 1 for the η_S values and Fig. 4 for the hole and electron density plots). Note that the CT (LE) character of the $S_0 \rightarrow S_1$ excitation is increased (reduced) in **CzAnCN** relative to **DPAAnCN**, because of the stronger localization of the hole over the carbazole moiety that is triggered by the slightly larger torsion between the donor and the acceptor moieties in the former molecule. This is in accordance with the calculated oscillator strength, f, of the $S_0 \rightarrow S_1$ transitions, larger in

Table 1 Hole and electron densities as obtained at the TDA/PBE0/6-31G(d,p) in the attachment/detachment formalism for **DPAAnCN** and **CzAnCN**

	Excited state	Energy/eV	η_S	Nature of state
DPAAnCN	T_1	1.76	0.85	LE
	S_1	2.50	0.42	HLCT
	T_2	2.52	0.58	HLCT
	T_3	3.35	0.86	LE
	S_2	3.36	0.88	LE
CzAnCN	T_1	1.86	0.88	LE
	T_2	2.59	0.34	HLCT
	S_1	2.61	0.26	HLCT
	T_3	3.00	0.22	HLCT
	S_2	3.02	0.14	CT

DPAAnCN (f = 0.13) than in **CzAnCN** (f = 0.03); high f values are necessary to achieve high Φ_{PL}.

As a result of the almost pure LE character of T_1 in both derivatives, our calculations yield a very large S_1–T_1 splitting energy, ΔE_{ST}, of 745 meV in **DPAAnCN** and 751 meV in **CzAnCN**, which are not compatible with a conventional RISC/TADF mechanism from thermalized triplets. However, a very small exergonic (endergonic) energy gap of 15 (16) meV was predicted going from T_2 to S_1 in **DPAAnCN** (**CzAnCN**), opening up the possibility for RISC *via* upper lying triplet states. Thus, in both **DPAAnCN** and **CzAnCN**, there is potential for a non-equilibrium process involving the quasi-degenerate S_1 and T_2 states to combine high exciton utilization efficiency and high Φ_{PL}, both of which would contribute to an enhancement of the external quantum efficiency in OLEDs (Fig. 4).

Photophysical properties

UV-Vis and transient PL measurements. Fig. 5 shows the UV-Vis absorption spectra in dichloromethane and the photoluminescence spectra in toluene of **DPAAnCN** and **CzAnCN**, with the data compiled in Tables 2 and 3. Both compounds possess a set of highly structured absorption bands from 370 to 412 nm that are characteristic of anthracene. **CzAnCN** shows a low intensity band at 436 nm assigned to a CT transition from Cz to AnCN. The CT band in **DPAAnCN** at 478 nm is much more intense and red-shifted compared to that of **CzAnCN** in agreement with the calculated S_1 energies (see Table 1). **DPAAnCN** and **CzAnCN** show broad and unstructured emission in toluene that are characteristic of an excited state with significant CT character. The photoluminescence maximum in **CzAnCN** is at 520 nm whereas for **DPAAnCN** it is red-shifted to 588 nm, which can be attributed to the stronger donor strength of the DPA moiety relative to Cz. Both compounds exhibit moderate photoluminescence quantum yields in toluene, Φ_{PL}, of 43% for **DPAAnCN** and 37% for **CzAnCN**, which decreased to 38% and 15%, respectively, upon exposure to air. Thin film measurements of **DPAAnCN** taken in a 10 wt% PMMA matrix show an enhanced Φ_{PL} of 57% coupled with a very small blue-shift in the PL spectrum (λ_{PL} = 580 nm, Fig. 8a) compared to that in toluene. For **CzAnCN** a similar blue-shift to 504 nm (Fig. 8a) was observed, but this was not accompanied by a change in Φ_{PL}. Transient photoluminescence measurements in toluene, as shown in Fig. 8b, revealed monoexponential decay for both compounds with lifetimes, τ_{PL}, of 30 ns for **DPAAnCN** and 20 ns for **CzAnCN** (Table 3). These results

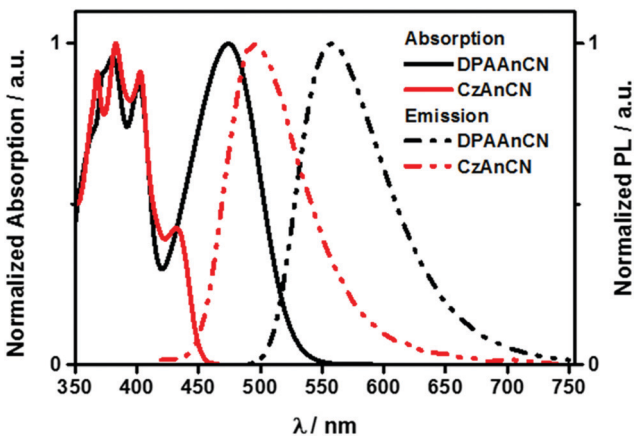

Fig. 5 UV-Vis absorption (in dichloromethane) and PL spectra of **DPAAnCN** and **CzAnCN** (in degassed toluene) at room temperature (λ_{exc} = 360 nm).

Table 3 Photophysical properties of **DPAAnCN** and **CzAnCN**

		DPAAnCN	CzAnCN
Hexane	λ_{PL}[a]/nm	506	452
	Φ_{PL}[b]/%	69.8 (47)	63.0 (28)
	τ_{PL}[e]/ns	26.3 (98%)	22.3 (99%)
		858 (2%)	760 (1%)
Toluene	λ_{PL}[a]/nm	588	520
	Φ_{PL}[b]/%	43.2 (37.5)	37 (14.7)
	τ_{PL}/ns	30.1	20
MeCN	λ_{PL}[a]/nm	638	581
	Φ_{PL}[b]/%	6.7 (6.3)	5.7 (2.9)
	τ_{PL}/ns	8.3	8.5
Thin film[c]	λ_{PL}/nm	580	504
	Φ_{PL}[d]/%	57	44
	τ_{PL}[e]/ns	29.5 (99%)	22.4 (99%)
		584.2 (1%)	228.6 (1%)

[a] Emission maxima reported from degassed solutions. [b] 0.5 M quinine sulfate in H_2SO_4 (aq) was used as the reference (Φ_{PL}: 54.6%).[25] Values quoted are in degassed solutions, which were prepared by five freeze–pump–thaw cycles. Values in parentheses are for aerated solutions, which were prepared by bubbling with air for 5 minutes. [c] Thin films were prepared by spin-coating 10 wt% doped samples in PMMA. [d] Values determined using an integrating sphere, degassing was done by N_2 purge. [e] Values in parentheses are the pre-exponential weighting factors.

Table 2 Absorption and electrochemical data of **CzAnCN** and **DPAAnCN**

Emitter	λ_{abs}[a]/nm, [$\varepsilon \times 10^{-4}/M^{-1}$ cm^{-1}]	Electrochemistry[b]/eV
CzAnCN	310 [0.29], 322 [0.45], 334 [0.63], 352 [0.46], 370 [0.87], 390 [0.91], 408 [0.84], 435(sh) [0.31]	HOMO: −5.99 LUMO: −3.15 ΔE: 2.84
DPAAnCN	343(sh) [0.23], 361(sh) [0.47], 373 [0.62], 381 [0.64], 402 [0.58], 472 [0.64]	HOMO: −5.68 LUMO: −3.20 ΔE: 2.48

[a] In DCM at 298 K. [b] In MeCN with 0.1 M [nBu$_4$N]PF$_6$ as the supporting electrolyte and Fc/Fc$^+$ as the internal reference (0.38 V *vs.* SCE).[22] The HOMO and LUMO energies were calculated using the relation $E_{HOMO/LUMO} = -(E^{ox}_{pa,1}/E^{red}_{pc,1} + 4.8)$ eV,[23] where E^{ox}_{pa} and E^{red}_{pc} are anodic and cathodic peak potentials, respectively. $\Delta E = -(E_{HOMO} - E_{LUMO})$.

indicate the absence of any delayed component to the emission decay that would be characteristic of TADF.

In order to probe the nature of the excited states in these compounds, we examined the effect of solvent polarity on the emission profiles. For **DPAAnCN**, the emission profiles remained unstructured, but grew broader as a function of solvent polarity (Fig. 6); a discernible shoulder exists in hexane, indicative of a HLCT behavior. Nearly analogous behavior is observed for **CzAnCN**; however, the emission profile in hexane is more structured, indicating an emission from a predominantly LE state in this solvent. Both compounds show a large positive solvatochromism as expected (λ_{PL} ranging from 515–638 nm for **DPAAnCN**, 453–581 nm for **CzAnCN**) in their excited states, which is a hallmark of emission from a CT state;[24] there is by contrast only a small positive solvatochromism in the ground state, as evidenced by the 5–10 nm range of values of λ_{abs} of the CT band in the absorption spectra (465–475 nm for **DPAAnCN**, 428–435 nm for **CzAnCN**). The marginally greater red-shift of the emission spectra in **CzAnCN** suggests that there is slightly greater CT character to the emissive S_1 state in this compound than in **DPAAnCN**, which is consistent with both the larger calculated η_S and a corresponding decrease in Φ_{PL} (Table 4).

To quantify the impact of solvent polarity on the nature of the excited state, we undertook a larger solvent polarity study with the aid of a Lippert–Mataga model,[24] which relates the Stokes shift to the solvent polarity factor, f, (Fig. 7 and Table S2, ESI‡). The slope of the fitted data provides insight into the dipole moment of the emissive S_1 state. For both **DPAAnCN** and **CzAnCN**, the Lippert–Mataga plots show two regimes, which indicates a change in the nature of the excited state. In low polarity solvents ($f < 0.1$), the dipole moments of the S_1 states of **DPAAnCN** and **CzAnCN** were estimated to be 9.5 D and 13.2 D, respectively. In higher polarity solvents ($f > 0.2$), the dipole moments of the emissive states increased to 25 D and 23 D for **DPAAnCN** and **CzAnCN**, respectively. We interpret this change in behavior to an increasing CT character of the emission in high polarity solvents while in low polarity solvents the S_1 state possesses more significant LE character. Indeed, gas phase TDA-DFT calculations show that the S_1 state in both compounds is best described as having HLCT character. Thus, in solvents of moderate polarity a ''hybrid state'' possessing significant LE and CT character is expected. This modulation in the nature of the excited state can be discerned from the transient PL spectra. In non-polar hexane, both compounds exhibited multiexponential emission decay with a dominant nanosecond component of 28 ns and 22 ns, respectively, for **DPAAnCN** and **CzAnCN**, and a minor sub-microsecond component of 858 ns and 760 ns, respectively, for **DPAAnCN** and **CzAnCN**. By contrast, in a moderately polar solvent such as toluene, only a single exponential emission lifetime of 30 ns and 20 ns was observed for **DPAAnCN** and **CzAnCN**, respectively. The transient PL decays in thin films resemble those measured in toluene, implying a similar hybrid emissive state in the solid-state (Fig. 8).

Time-resolved electron paramagnetic resonance. In order to investigate in detail the nature of the excited triplet states predicted by TDA-DFT calculations of **DPAAnCN** and **CzAnCN** we carried out time-resolved EPR (TREPR) spectroscopy with microsecond time resolution. Thanks to its high sensitivity and selectivity, TREPR spectroscopy is well suited to detect and

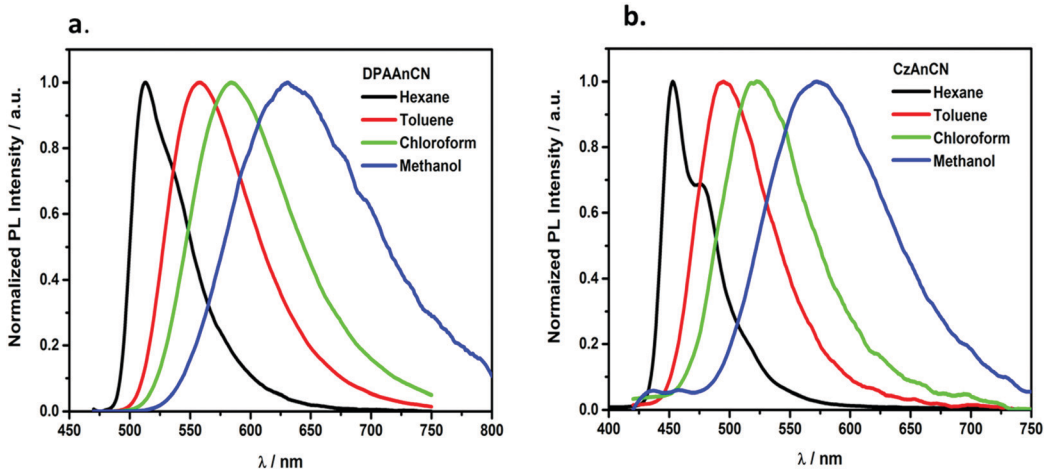

Fig. 6 Solvatochromic PL spectra of (a) **DPAAnCN** and (b) **CzAnCN** (λ_{exc} = 360 nm).

Table 4 Summary of electroluminescence properties for devices based on **DPAAnCN** and **CZAnCN**

Device (emitter)	V_{on}[a]/V	λ_{EL}[b]/nm	Luminance$_{max}$/cd m^{-2}	EQE$_{max}$[c] (@ 100 cd m^{-2})/%	CE$_{max}$[c]/cd A^{-1}	PE$_{max}$[c]/lm W^{-1}	CIE[d]/(x,y)
Device VA (DPAAnCN)	3.4	570	11230	6.0 (5.5)	19.0	12.9	(0.42, 0.46)
Device VB (CzAnCN)	3.2	510	8450	4.0 (3.5)	12.0	9.0	(0.25, 0.48)

[a] Measured at 1 cd m^{-2}. [b] Emission maxima at 1 mA cm^{-2}. [c] Maximum efficiencies at 1 cd m^{-2}. [d] Commission Internationale de l'Éclairage coordinates at 1 mA cm^{-2}.

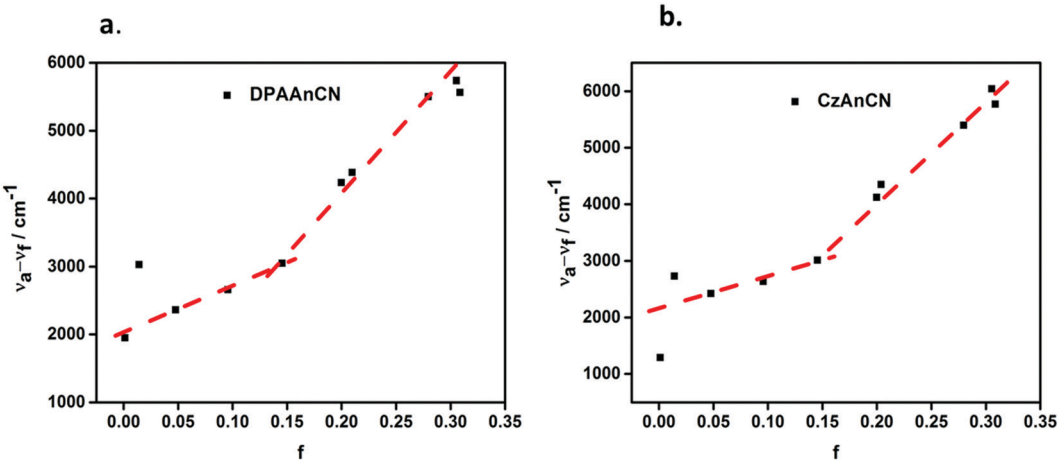

Fig. 7 Solvatochromic Lippert–Mataga plots of (a) **DPA-AnCN** and (b) **CzDPA-AnCN**.

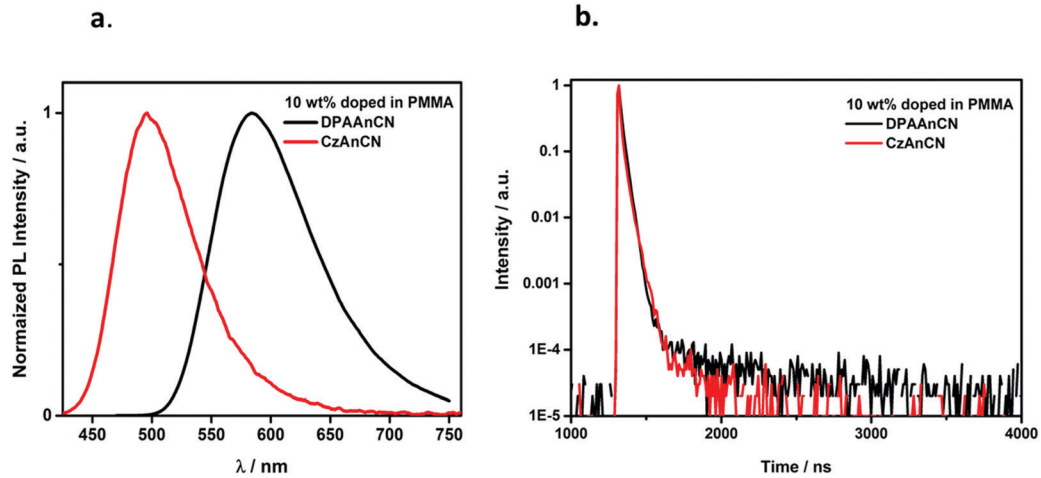

Fig. 8 (a) PL spectra and (b) transient PL decay curves of **DPAAnCN** and **CzAnCN** in 10 wt% doped PMMA films (λ_{exc} = 378 nm).

unambiguously distinguish different triplet states.[26] In Fig. S3 (ESI‡) we report the TREPR spectra acquired at 80 K after a visible laser pulse on samples of **DPAAnCN** and **CzAnCN** in toluene solution. Both spectra are composed of a broad band extending for about 1200 Gauss with a peculiar absorptive/emissive character typical of excited triplet states generated by intersystem crossing (ISC).

By performing the best-fit spectral simulations of both spectra, we obtain the *D* and *E* parameters, which define the dipolar interaction between the two unpaired electrons of the triplet state (Table S3, ESI‡).[27] In particular, the *D* value is inversely proportional to the average distance of the unpaired electrons of the triplet state and can therefore provide information regarding triplet state delocalization. In **DPAAnCN**, from the simulation we observe the presence of two triplet excited states, a localized one (*D* = 610 Gauss, red line) and a delocalized one (*D* = 245 Gauss, green line). We can attribute the localized triplet to the calculated T_1 state, which has essentially a LE character (hole-electron densities overlap η_S larger than 0.8 for both compounds), while the delocalized triplet state is associated to the calculated T_2 state, which has a HLCT character and whose unpaired electrons are on average more distant (ϕ_S = 0.58). In the **CzAnCN** sample, a broad and intense signal with a *D* value of 690 Gauss is observed that is associated with the LE T_1 state. The T_2 triplet is not detectable *via* TREPR either due to its fast decay time compared to TREPR time resolution or its much lower intensity compared to T_1 state.

The TREPR analysis corroborates the nature of the T_1 and T_2 triplet states predicted by calculations and confirms that the transition between S_1 and T_2 is feasible and not symmetry forbidden thereby suggesting an alternative pathway for RISC from the T_2 state.

Electrochemical properties

The electrochemical behavior of **DPAAnCN** and **CzAnCN** was studied by cyclic voltammetry in degassed acetonitrile with tetrabutylammonium hexafluorophosphate as the supporting electrolyte. The cyclic voltammograms (CVs) are shown in Fig. 9 and the data are summarized in Table 2. Both emitters exhibit highly reversible reduction waves associated with the cyanoanthracene moiety. The increased conjugation of the DPA donor influences the reduction potential slightly, pushing it

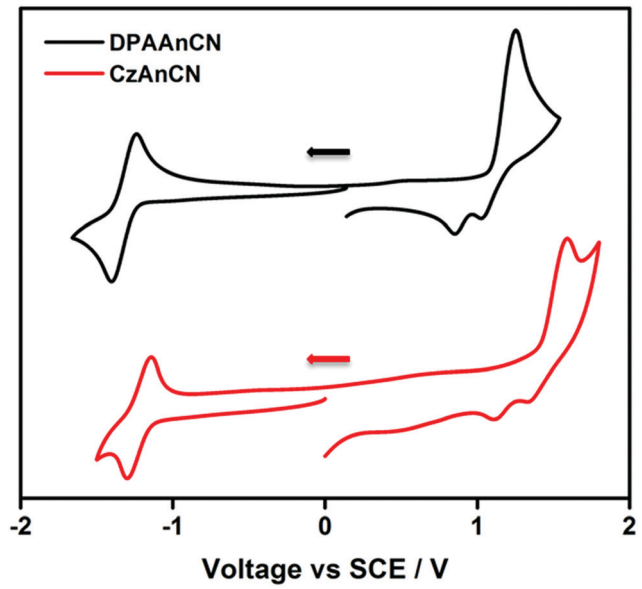

Fig. 9 Cyclic voltammograms of **DPAAnCN** and **CzAnCN** in degassed MeCN (scan rate: 100 mV s^{-1}).

cathodically from −1.22 V for **CzAnCN** to −1.27 V for **DPAAnCN**. The oxidation waves of **DPAAnCN** and **CzAnCN** were found to be irreversible. This is not surprising as the carbazole radical cation has been reported to be electrochemically unstable and undergoes dimerization.[28] Similarly, the DPA group has been shown to exhibit irreversible oxidation.[29] By changing the donor strength, the HOMO levels (−5.68 eV for **DPAAnCN** and −5.99 eV for **CzAnCN**) can be moderately tuned as would be expected, resulting in electrochemical gaps of 2.84 and 2.48 eV, respectively, for **CzAnCN** and **DPAAnCN**.

Electroluminescent devices

Based on the promising photophysical properties for **DPAAnCN** and **CzAnCN** in PMMA doped thin films, we fabricated vacuum-deposited multilayer organic light emitting diodes (OLEDs). The optimum doping concentration and appropriate hosts were assessed by absolute Φ_{PL} measurements (Table S4, ESI‡). Vacuum-deposited 10 wt% doped films of **DPAAnCN** and **CzAnCN** in mCP [1,3-bis(carbazol-9-yl)benzene] exhibited Φ_{PL} of 56% and 45%, respectively. Energy level diagrams and chemical structures of all the materials used in the device fabrication are shown in Fig. 10. For the OLED (Device VA) with **DPAAnCN** as the emitter, the following architecture was employed: ITO/NPB (50 nm)/**DPAAnCN**:mCP (10 wt%, 20 nm)/TPBi (50 nm)/LiF (1 nm)/Al (100 nm), where *N*,*N*′-bis(naphthalen-1-yl)-*N*,*N*′-bis(phenyl)benzidine (NPB) was used as a hole transporting layer (HTL), mCP was used as a host material and 2,2′,2″-(1,3,5-benzinetriyl)-tris(1-phenyl-1-*H*-benzimidazole) (TPBi) was used as an electron transporting layer (ETL). mCP has been widely used as a host material due to its sufficiently high lying triplet state (2.9 eV).[30] For the OLED (Device VB) with **CZAnCN** as the emitter, a modified device architecture was used: ITO/NPB (30 nm)/TCTA (20 nm)/mCP (10 nm)/**CzAnCN**:mCP (10 wt%, 20 nm)/DPEPO (10 nm)/TPBi (50 nm)/LiF (1 nm)/Al (100 nm), where tris(4-carbazoyl-9-ylphenyl)amine (TCTA) was incorporated as an additional hole transporting and electron blocking layer. For this device we used electron and hole blocking layers comprised of mCP and DPEPO [(bis[2-(diphenylphosphino)phenyl]]ether oxide] respectively, in order to confine the exciton recombination zone within the EML.

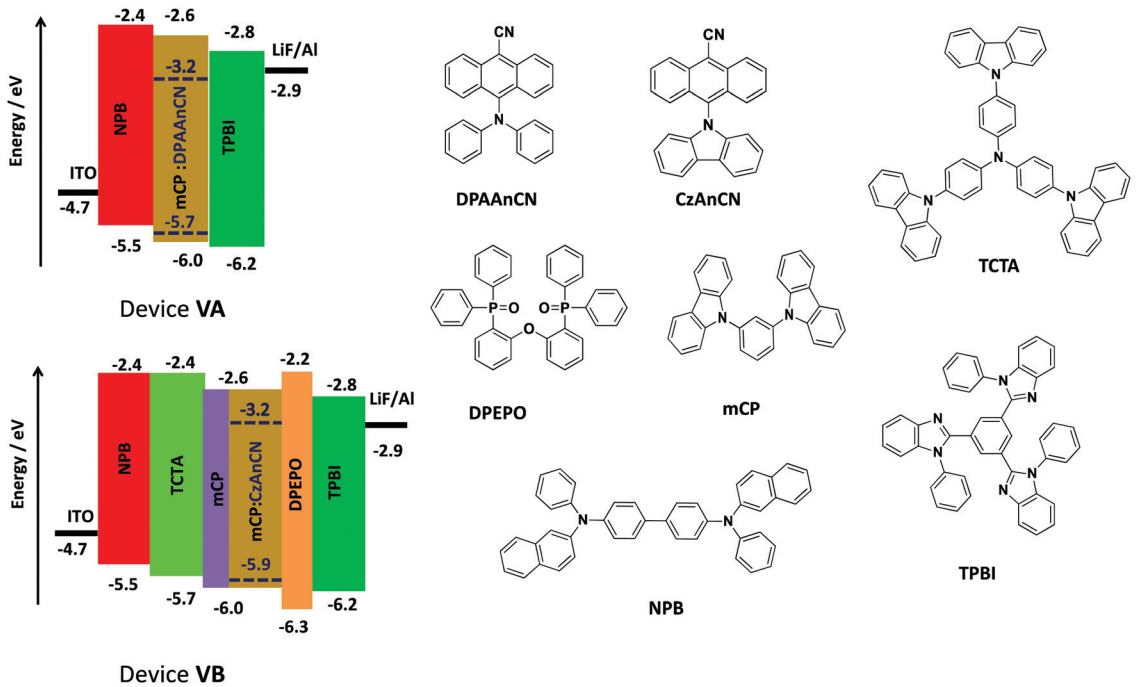

Fig. 10 Device architecture and chemical structures of the materials used.

The electroluminescence properties of the vacuum-deposited devices are shown in Fig. 11 and the performances are summarized in Table 4. Device VA exhibited yellow emission with λ_{EL} of 570 nm and CIE coordinates of (0.42, 0.46) while device VB showed a sky-blue emission with λ_{EL} of 510 nm and CIE coordinates and (0.25, 0.48). Device VA exhibited excellent performance, with a maximum current efficiency of 19.0 cd A^{-1}, power efficiency of 12.9 lm W^{-1}, and EQE_{max} of 6.0% (5.5% at 100 cd m^{-2}). A low turn-on voltage of 3.4 V and a maximum luminance of 11 230 cd m^{-2} were observed. Device VB performed less well, giving a maximum current efficiency of 12.0 cd A^{-1}, power efficiency of 9.0 lm W^{-1} and EQE_{max} of 4.0% (3.5% at 100 cd m^{-2}). A comparably low turn-on voltage of 3.2 V and a reduced maximum luminance of 9000 cd m^{-2} were also observed. The superior performance of device VA, employing **DPAAnCN** as the emitter, exceeds the theoretical limit for the EQE (5%) in a fluorescent-emitter OLED, which implicates the utilization of both singlet and triplet excitons. Device VA exhibited a low efficiency roll-off, implying low rates of TTA and TPA in the device. Device VB exhibited a relatively lower turn-on voltage and higher current densities as compared to Device VA, which could be attributed to better charge transport in Device VB due to the intermediate TCTA layer reducing the hole injection barrier between the HOMOs of NPB and mCP (Fig. 10). The performance of Device VA is amongst the best performing HLCT OLEDs, particularly for yellow/red emitters. Moreover, such a high EQE_{max} was obtained by using a simple three-layered device architecture. To the best of our knowledge, only **NZ2Ac** (Fig. 1) shows a slightly better EQE_{max} of 6.2% amongst the reported yellow/red HLCT emitters.[13] However, this higher EQE_{max} for **NZ2Ac** required a more complex multilayer device architecture.

Assuming a recombination efficiency of unity, an outcoupling efficiency, Φ_{out} of 20% and taking Φ_{PL} of 56% in mCP, Device VA exhibited an exciton utilization efficiency, Φ_s, of 54%, which is far superior to the upper limit of 25% implicated for a fluorescent molecule according to spin statistics. Using the same approach, Device VB exhibited Φ_s of 45%, likewise greater than the maximum expected for an OLED based on a fluorescent molecule. In order to explain the reason behind the high exciton utilization efficiency in the OLEDs using **DPAAnCN** and **CzAnCN**, we evaluated whether these compounds were emitting *via* either TTA or TADF in the device. The pseudo-linear relationship between luminance and current density (Fig. 11d) demonstrated that TTA is not operational in the devices. Temperature-dependent transient PL measurements of **DPAAnCN** and **CzAnCN** (10 wt% doped in mCP) did not show any enhancement in the delayed component of the emission decay (Fig. S2, ESI‡). This, coupled with a ΔE_{ST} of *ca.* 0.75 eV and a nearly similar T_1–T_2 energy difference for both compounds as predicted by theoretical calculations, ruled out the possibility of TADF.

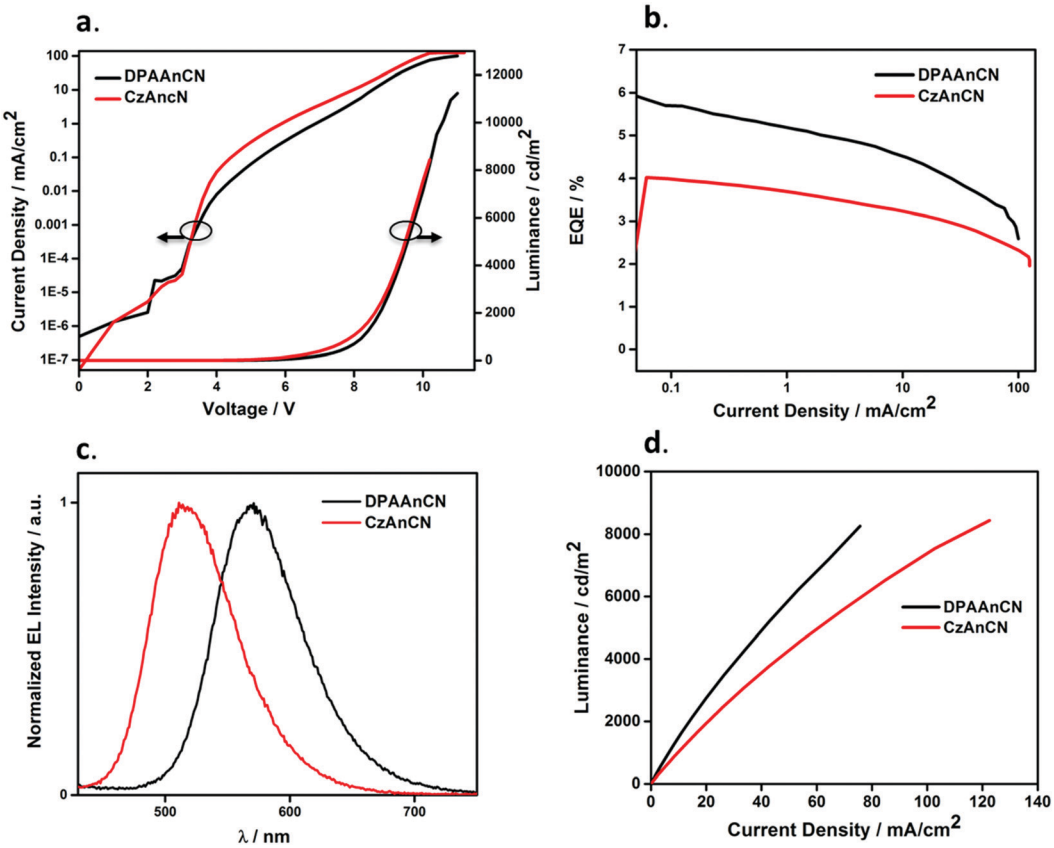

Fig. 11 (a) Current density–voltage-luminance characteristics; (b) EQE *vs.* current density; (c) normalized EL spectra; and (d) luminance *vs.* current density characteristics of vacuum-processed EL devices with **DPAAnCN** (Device VA) and **CzAnCN** (Device VB) as emitters.

We next explored whether the enhanced EQE was the result of improved light outcoupling due to non-isotropic orientation of the emitters within the emissive layer. We performed angle-resolved PL spectroscopy of thin films of 10 wt% doped **DPAAnCN** and **CzAnCN** in mCP vacuum-deposited on glass substrates (more information about these measurements in the ESI‡).[31] These measurements revealed an isotropic orientation of both emitters in the films, and thus there is no enhanced light outcoupling and $\Phi_{out} \sim 20\%$ can be assumed (Fig. S14, ESI‡).

We therefore propose that the enhanced exciton utilization stems from a non-equilibrium RISC process involving a higher-lying triplet excited state in resonance with S_1. Upon recombination of holes and electrons within the EML, both singlet and triplet excitons form and normally, in a dense manifold of singlet or triplet excitons, these excitons rapidly and non-radiatively decay *via* IC to either the S_1 or T_1 states, respectively. However, if the energy difference between higher-lying triplet states (T_n) and a corresponding singlet excited state is sufficiently small, as is the case for HLCT states, and the transition between the two is not symmetry-forbidden (El-Sayed's rule),[32] then RISC can conceivably compete with IC (Fig. 4),[33] providing a pathway for triplet exciton utilization despite a large $\Delta E_{S_1-T_1}$.[34] TDA-DFT calculations for both **DPAAnCN** and **CzAnCN** show that $\Delta E(T_2–T_1)$ is large while $\Delta E(T_2–S_1)$ is vanishingly small, and that each of these states possesses a different degree of mixed CT and LE (HLCT) character thereby mitigating the constraints imposed by El Sayed's rule leading to non-vanishing spin–orbit coupling. Though we have no direct experimental evidence for the hot exciton channel mechanism, our computational results indicate that the two compounds fulfil the energetic requirements for a T_2 to S_1 intersystem crossing competing with the spin-conserving T_2 to T_1 internal conversion. This result is further corroborated by TREPR spectroscopy, which shows that the ISC pathway from S_1 to T_2 is allowed. In view of the high exciton utilization efficiency observed and after having ruled out other possible mechanisms such as TADF, TTA and enhanced light outcoupling, we conclude that the hot RISC process should occur on shorter or comparable timescales than energy relaxation in the triplet manifold. This is an unusual finding that is expected to be specific to the molecular architectures studied here and deserves further (kinetic) studies.

Concluding remarks

We have synthesized and characterized two new emitters bearing a cyanoanthracene acceptor core and either DPA or Cz donors. Vacuum-deposited devices exhibited excellent performance with exciton utilization efficiencies $> 50\%$ and $EQE_{max} > 5\%$, largely surpassing the spin statistics limits. These are very unexpected results, as both conventional TADF from the thermalized triplet population and triplet–triplet annihilation are inactive, very likely owing to an unfavourable S_1–T_1 energy gap. In contrast, our computational work and TREPR analysis suggest that a higher-lying T_2 triplet excited state with HLCT character could be involved in the reversible singlet-to-triplet conversion. We thus speculate that a "hot exciton" channel is operational here, which rests on the hypothesis that RISC from T_2 to S_1 outcompetes internal conversion from the largely energetically spaced T_1 and T_2 states. In favour of this hypothesis, we note that the slightly different nature of the T_2 and S_1 excited states and their quasi degeneracy should prompt high spin conversion rates. It is also likely that internal relaxation from T_2 to T_1 is slowed down by the different equilibrium geometries of the two triplet states associated with their very different character, besides their large energy separation. Namely, the non-radiative recombination could possibly proceed through a conical intersection involving a large amplitude torsional relaxation, which would be hindered in the solid as characterized by a too large activation energy. We are currently exploring these hypotheses, combining *ab initio* surface potentials and non-adiabatic molecular dynamics simulations (to model triplet internal conversion) with pump–probe spectroscopy. Irrespective of the outcome of the ongoing investigations, we conclude that the grafting of the cyano group onto the anthracene-based acceptor in **DPAAnCN** and **CzAnCN** is key to prompt the formation of HLCT states and to drive a Jablonski energy diagram offering potential for hot exciton processes to bypass spin statistics for singlet emission.

Conflicts of interest

A patent has been filed. PCT/GB2015/054171, filed Dec. 29, 2015.

Acknowledgements

E. Z.-C. acknowledges the University of St Andrews and the Leverhulme Trust (RPG-2016-047) for financial support. E. Z.-C. and I. D. W. S. thank EPSRC (EP/P010482/1) for support. We thank the EPSRC UK National Mass Spectrometry Facility at Swansea University for analytical services. The work in Mons was supported by the European Union's Horizon 2020 research and innovation program under Grant Agreement No. 646176 (EXTMOS project). Computational resources have been provided by the Consortium des Équipements de Calcul Intensif (CÉCI), funded by the Fonds de la Recherche Scientifiques de Belgique (F.R.S.-FNRS) under Grant No. 2.5020.11. C. M. and G. C. acknowledge funding by the European Commission through a Marie Skłodowska Curie fellowship (No. 703387 and 799302, respectively). M. C. G. acknowledges funding from EPSRC (EP/R010595/1). D. B. is a FNRS Research Director. Y. O. acknowledges fruitful discussions with Prof. Juan-Carlos Sancho-Garcia from the University of Alicante and Prof. Luca Muccioli from the University of Bologna. A. P. acknowledges the European Union's Horizon 2020 research and innovation programme under Marie Sklodowska Curie Grant agreement No. 722651 (SEPOMO project). EPR measurements were performed in the Centre for Advanced ESR (CAESR), located in the Department of Chemistry of the University of Oxford, and this work was supported by the EPSRC (EP/L011972/1). A. P. thanks Prof. Moritz Riede, University of Oxford, for support and fruitful discussions and Dr William Myers, CAESR facility, for his kind assistance with the EPR measurements.

References

1 M. Pope, H. P. Kallmann and P. Magnante, *J. Chem. Phys.*, 1963, **38**, 2042.
2 C. W. Tang and S. A. VanSlyke, *Appl. Phys. Lett.*, 1987, **51**, 913–915.
3 S.-J. Su, E. Gonmori, H. Sasabe and J. Kido, *Adv. Mater.*, 2008, **20**, 4189–4194.
4 (*a*) M. A. Baldo, D. F. O'Brien, Y. You, A. Shoustikov, S. Sibley, M. E. Thompson and S. R. Forrest, *Nature*, 1998, **395**, 151–154; (*b*) M. A. Baldo, S. Lamansky, P. E. Burrows, M. E. Thompson and S. R. Forrest, *Appl. Phys. Lett.*, 1999, **75**, 4.
5 (*a*) J. Partee, E. L. Frankevich, B. Uhlhorn, J. Shinar, Y. Ding and T. J. Barton, *Phys. Rev. Lett.*, 1999, **82**, 3673–3676; (*b*) J. Partee, E. L. Frankevich, B. Uhlhorn, J. Shinar, Y. Ding and T. J. Barton, *Phys. Rev. Lett.*, 1999, **82**, 3673–3676.
6 (*a*) H. Uoyama, K. Goushi, K. Shizu, H. Nomura and C. Adachi, *Nature*, 2012, **492**, 234–238; (*b*) M. Y. Wong and E. Zysman-Colman, *Adv. Mater.*, 2017, **29**, 1605444.
7 C. Murawski, K. Leo and M. C. Gather, *Adv. Mater.*, 2013, **25**, 6801–6827.
8 (*a*) W. Li, D. Liu, F. Shen, D. Ma, Z. Wang, T. Feng, Y. Xu, B. Yang and Y. Ma, *Adv. Funct. Mater.*, 2012, **22**, 2797–2803; (*b*) W. Li, Y. Pan, L. Yao, H. Liu, S. Zhang, C. Wang, F. Shen, P. Lu, B. Yang and Y. Ma, *Adv. Opt. Mater.*, 2014, **2**, 892–901.
9 (*a*) W. Li, Y. Pan, R. Xiao, Q. Peng, S. Zhang, D. Ma, F. Li, F. Shen, Y. Wang, B. Yang and Y. Ma, *Adv. Funct. Mater.*, 2014, **24**, 1609–1614; (*b*) S. Zhang, L. Yao, Q. Peng, W. Li, Y. Pan, R. Xiao, Y. Gao, C. Gu, Z. Wang, P. Lu, F. Li, S. Su, B. Yang and Y. Ma, *Adv. Funct. Mater.*, 2015, **25**, 1755–1762.
10 D. Hu, L. Yao, B. Yang and Y. Ma, *Philos. Trans. R. Soc., A*, 2015, **373**, 20140318.
11 R. Kumar Konidena, K. R. Justin Thomas, D. Kumar Dubey, S. Sahoo and J. H. Jou, *Chem. Commun.*, 2017, **53**, 11802–11805.
12 C. Wang, X. Li, Y. Pan, S. Zhang, L. Yao, Q. Bai, W. Li, P. Lu, B. Yang, S. Su and Y. Ma, *ACS Appl. Mater. Interfaces*, 2016, **8**, 3041–3049.
13 T. Liu, L. Zhu, S. Gong, C. Zhong, G. Xie, E. Mao, J. Fang, D. Ma and C. Yang, *Adv. Opt. Mater.*, 2017, **5**, 1700145.
14 J. Zhao, B. Liu, Z. Wang, Q. Tong, X. Du, C. Zheng, H. Lin, S. Tao and X. Zhang, *ACS Appl. Mater. Interfaces*, 2018, **10**, 9629–9637.
15 J. Yang, Q. Guo, J. Wang, Z. Ren, J. Chen, Q. Peng, D. Ma and Z. Li, *Adv. Opt. Mater.*, 2018, **6**, 1800342.
16 C. Fu, S. Luo, Z. Li, X. Ai, Z. Pang, C. Li, K. Chen, L. Zhou, F. Li, Y. Huang and Z. Lu, *Chem. Commun.*, 2019, **55**, 6317–6320.
17 Y. Xu, X. Liang, X. Zhou, P. Yuan, J. Zhou, C. Wang, B. Li, D. Hu, X. Qiao, X. Jiang, L. Liu, S.-J. Su, D. Ma and Y. Ma, *Adv. Mater.*, 2019, **31**, 1807388.
18 (*a*) M. Bian, Z. Zhao, Y. Li, Q. Li, Z. Chen, D. Zhang, S. Wang, Z. Bian, Z. Liu, L. Duan and L. Xiao, *J. Mater. Chem. C*, 2018, **6**, 745–753; (*b*) J. Zhang, Y. Zhao, H. Xu, D. Zhang, Y. Miao, R. Shinar, J. Shinar, H. Wang, B. Xu and Y. Wu, *J. Mater. Chem. C*, 2019, **7**, 10810–10817.
19 (*a*) J. P. Perdew, M. Ernzerhof and K. Burke, *J. Chem. Phys.*, 1996, **105**, 9982–9985; (*b*) C. Adamo and V. Barone, *J. Chem. Phys.*, 1999, **110**, 6158–6170.
20 (*a*) S. Grimme, *Chem. Phys. Lett.*, 1996, **259**, 128–137; (*b*) S. Hirata and M. Head-Gordon, *Chem. Phys. Lett.*, 1999, **314**, 291.
21 M. Moral, L. Muccioli, W. J. Son, Y. Olivier and J. C. Sancho-García, *J. Chem. Theory Comput.*, 2015, **11**, 168–177.
22 V. V. Pavlishchuk and A. W. Addison, *Inorg. Chim. Acta*, 2000, **298**, 97–102.
23 C. M. Cardona, W. Li, A. E. Kaifer, D. Stockdale and G. C. Bazan, *Adv. Mater.*, 2011, **23**, 2367–2371.
24 Z. R. Grabowski, K. Rotkiewicz and W. Rettig, *Chem. Rev.*, 2003, **103**, 3899–4032.
25 W. H. Melhuish, *J. Phys. Chem.*, 1961, **65**, 229–235.
26 T. Biskup, *Front. Chem.*, 2019, **7**, 10.
27 M. Righetto, A. Privitera, F. Carraro, L. Bolzonello, C. Ferrante, L. Franco and R. Bozio, *Nanoscale*, 2018, **10**, 11913–11922.
28 A. Tomkeviciene, J. V. Grazulevicius, D. Volyniuk, V. Jankauskas and G. Sini, *Phys. Chem. Chem. Phys.*, 2014, **16**, 13932–13942.
29 L. Xu, H. Zhu, G. Long, J. Zhao, D. Li, R. Ganguly, Y. Li, Q.-H. Xu and Q. Zhang, *J. Mater. Chem. C*, 2015, **3**, 9191–9196.
30 (*a*) S. H. Kim, J. Jang and J. Y. Lee, *Appl. Phys. Lett.*, 2007, **90**, 223505; (*b*) Y. Tao, C. Yang and J. Qin, *Chem. Soc. Rev.*, 2011, **40**, 2943–2970.
31 (*a*) P. Liehm, C. Murawski, M. Furno, B. Lüssem, K. Leo and M. C. Gather, *Appl. Phys. Lett.*, 2012, **101**, 253304; (*b*) A. Graf, P. Liehm, C. Murawski, S. Hofmann, K. Leo and M. C. Gather, *J. Mater. Chem. C*, 2014, **2**, 10298–10304.
32 M. A. El-Sayed, *J. Chem. Phys.*, 1963, **38**, 2834–2838.
33 W. Barford, R. J. Bursill and D. V. Makhov, *Phys. Rev. B: Condens. Matter Mater. Phys.*, 2010, **81**, 035206.
34 (*a*) M. Segal, M. Singh, K. Rivoire, S. Difley, T. Van Voorhis and M. A. Baldo, *Nat. Mater.*, 2007, **6**, 374–378; (*b*) S. Difley, D. Beljonne and T. Van Voorhis, *J. Am. Chem. Soc.*, 2008, **130**, 3420–3427.